TU Delft

Delft University of Technology

Boundary layer transition induced by roughness arrays over NACA 0012 airfoil

Ye, Qingqing; Avallone, Francesco; Ragni, Daniele; Casalino, Damiano

DOI
10.1016/j.expthermflusci.2025.111505

Publication date
2025

Document Version
Final published version

Published in
Experimental Thermal and Fluid Science

Citation (APA)
Ye, Q., Avallone, F., Ragni, D., & Casalino, D. (2025). Boundary layer transition induced by roughness arrays over NACA 0012 airfoil. *Experimental Thermal and Fluid Science*, *168*, Article 111505. https://doi.org/10.1016/j.expthermflusci.2025.111505

Important note
To cite this publication, please use the final published version (if applicable).
Please check the document version above.

Copyright
Other than for strictly personal use, it is not permitted to download, forward or distribute the text or part of it, without the consent of the author(s) and/or copyright holder(s), unless the work is under an open content license such as Creative Commons.

Takedown policy
Please contact us and provide details if you believe this document breaches copyrights.
We will remove access to the work immediately and investigate your claim.

This work is downloaded from Delft University of Technology.
For technical reasons the number of authors shown on this cover page is limited to a maximum of 10.

Green Open Access added to TU Delft Institutional Repository

'You share, we take care!' - Taverne project

https://www.openaccess.nl/en/you-share-we-take-care

Otherwise as indicated in the copyright section: the publisher is the copyright holder of this work and the author uses the Dutch legislation to make this work public.

Experimental Thermal and Fluid Science 168 (2025) 111505

Contents lists available at ScienceDirect

Experimental Thermal and Fluid Science

journal homepage: www.elsevier.com/locate/etfs

Boundary layer transition induced by roughness arrays over NACA 0012 airfoil

Qingqing Ye [a,*], Francesco Avallone [b], Daniele Ragni [c], Damiano Casalino [c]

[a] State Key Laboratory of Fluid Power and Mechatronic Systems, Department of Mechanics, Zhejiang University, Hangzhou, 310027, PR China
[b] Department of Mechanical and Aerospace Engineering, Politecnico di Torino, Torino, 10129, Italy
[c] Faculty of Aerospace Engineering, Delft University of Technology, Delft, 2629HS, The Netherlands

ARTICLE INFO

Keywords:
Boundary layer flow
Arrays of roughness elements
Laminar to turbulent transition

ABSTRACT

Laminar to turbulent transition induced by spanwise periodic arrays of cylindrical roughness elements over a NACA 0012 airfoil is investigated by hotwire anemometry and infrared thermography. The roughness elements are placed in the flow under adverse pressure gradient. Three configurations are investigated, namely an isolated roughness element, a spanwise array of roughness elements, and a pair of arrays in stagger. The streamwise and spanwise interactions between roughness wakes are addressed, focusing on the evolution of mean flow features and mechanisms for the subsequent process of laminar-turbulent transition. The spanwise interaction between roughness elements involves the connections and merging of neighboring low-speed regions (MLS) in the wake, which affects the spanwise distribution and amplitude of the velocity streaks. The maximum effect on promoting transition is observed when two neighboring low-speed regions overlap with each other in the near wake (within 6 times roughness height). The addition of a second roughness array promotes transition when the spanwise spacing is larger than two times the roughness diameter. Spectral analysis of the streamwise velocity fluctuations reveals that the number of roughness elements within the spanwise array affects the number of MLSs and the dominant instability mechanism. For an odd number of MLSs, the Kelvin–Helmholtz instability dominates the growth of velocity fluctuations around the three-dimensional shear layers. For an even number of MLSs, both Kelvin–Helmholtz and asymmetric instabilities appear in the wake. In this case, the dominant mode that leads to transition depends on the spanwise spacing between roughness elements.

1. Introduction

Understanding the role of surface roughness on transition has been a challenging topic for researchers in the past decades [1]. The three-dimensional roughness element induces mean flow modification, which can act as a catalyst for receptivity to external disturbances, change the growth characteristics of existing instability waves, or even lead to self-sustained unsteadiness via global instability [2,3]. The three-dimensional roughness elements are usually categorized into isolated and distributed types. Realistic surface roughness, such as surface non-uniformities due to the ablation of the thermal protection system during hypersonic re-entry [4], icing over aircraft wings [5], and degradation over the turbine blades [6,7], commonly involves complex distributed patterns. The induced transition mechanisms are more challenging to understand due to the spatial interaction between flow structures in comparison with an isolated element.

For three-dimensional roughness elements, one of the main flow features is the formation of counter-rotating pairs of streamwise vortices in the roughness wake, which generate low- and high-speed streaks that modulate the shear layer along both the wall-normal and spanwise directions [8,9]. A possible mechanism underlying the forced transition due to surface roughness involves the transient growth theory, in which the stationary streamwise vortices in the near wake induce disturbances that undergo maximum energy growth over a finite spatial distance [10,11]. In this case, the formation of velocity streaks through the 'lift-up' mechanism takes over the role of Tollmien-Schlichting (TS) waves in the growth of the perturbations [12]. When the streak amplitude exceeds a critical value, the flow can support an unsteady secondary instability that leads to either varicose (symmetric) or sinuous (asymmetric) modulation of the streak structure, eventually promoting transition to turbulence [13].

Past studies have dealt with the transition induced by isolated roughness elements, focusing on the evolution of unstable velocity

* Corresponding author.
E-mail address: qingqing_ye@zju.edu.cn (Q. Ye).

https://doi.org/10.1016/j.expthermflusci.2025.111505
Received 11 December 2024; Received in revised form 22 March 2025; Accepted 22 April 2025
Available online 5 May 2025
0894-1777/© 2025 Elsevier Inc. All rights are reserved, including those for text and data mining, AI training, and similar technologies.

streaks. Choudhari and Fischer [14] performed numerical simulations to study the growth of disturbances induced by a spanwise array of circular cylinders. The onset of bypass transition is preceded by the formation of self-sustained vortex shedding behind the cylinders close to the centerline on top of the low-speed region. Chang et al. [15] found that the onset of instability can be concentrated on the low-speed streak both along the centerline and at the sideward. The latter is associated with the horseshoe vortices formed in the separated flow region upstream of the cylinder. Ye et al. [16,17,18] studied the three-dimensional transitional flow features behind isolated roughness elements using tomographic particle image velocimetry (PIV). For cylindrical roughness element, the inflectional velocity profiles over the sideward low-speed regions lead to the generation of hairpin vortices. The former structure plays a key role in the inception of the flow instability and turbulent fluctuations, leading to transition.

For distributed roughness elements, the interaction between flow structures induced by different portions of a distributed pattern can modulate the velocity streak distribution and influence both the streamwise growth in disturbance amplitudes and the eventual route to transition [19]. Drews et al. [20] investigated the wake topology of quasi-random, distributed roughness patches on a flat plate using direct numerical simulation (DNS). The tallest roughness element within the patch was found to control the vorticity distribution in the wake. The number of streamwise vortices was affected by the roughness geometry. They observed a single streamwise vortex behind an asymmetric roughness distribution and counter-rotating pairs of streamwise vortices in the case of symmetric roughness distributions. von Deyn et al. [19] numerically studied the instability mode developed over velocity streaks in the wake of distributed roughness elements. They found that the breakdown to turbulence is related to the growth of sinuous instability over low-speed streaks. To further understand the interaction between flow structures and transition mechanisms induced by different parts of the roughness patch, distributions that are spatially non-localized but fully deterministic in nature were studied. Muppidi and Mahesh [21] studied the onset of transition in the presence of a sinusoidal roughness distribution in both streamwise and spanwise directions by using DNS for a supersonic, flat plate boundary layer (Mach 2.9). Counter-rotating streamwise vortices are generated over the peaks in the roughness region. These vortices convected downstream with growing strength due to the interaction with the peaks of the downstream roughness elements. The streamwise vortices destabilized the detached shear layer, eventually leading to the onset of laminar-turbulent transition and a breakdown into turbulence. Following similar roughness distribution, Choudhari et al. [22] extended the work on disturbance growth over the three-dimensional roughness patch using stability analysis. A fundamental asymmetric mode type is found to sustain the amplification of disturbances both above and in the wake of the roughness.

Despite the extensive research, the parameter space associated with the distributed roughness elements is large, including spacial proximity, size, and orientation. The parameter variations could change the overall flow topology and velocity streak distribution above and in the wake of the elements, affecting the selection of dominant instability mode leading to transition. In order to separate the effects of interactions due to streamwise and spanwise proximity between roughness elements, the distributed roughness configurations are obtained by using arrays of isolated roughness elements. Several studies have been performed to understand the streamwise interaction between isolated roughness elements. The effect of streamwise spacing remains controversial. Carmichael [23] experimentally studied the transition effect induced by roughness arrays. When the streamwise spacing between the elements is larger than three diameters, the interaction is considered negligible. Choudhari et al. [2] studied the interaction of two diamond-shaped roughness elements aligned in tandem in a supersonic, flat plate boundary layer of three diameters apart using DNS. Compared with isolated roughness, tandem arrays of roughness elements led to an augmentation of the velocity streak amplitude in the wake. The increase in streak amplitude is less evident for the taller roughness elements. Chou et al. [24] studied the streamwise interaction of several tandem cylinders using hotwire anemometry at Mach 3.5. Symmetric type of instability mode is produced in the wake of the tall cylinders. The maximum disturbance growth is established when two cylinders are spaced four diameters apart in the streamwise direction, which is contrary to the result of Carmichael [23]. For smaller spacing, the effect on transition is trivial. In the incompressible flow, Ma and Mahesh [25] performed DNS of distributed roughness elements with predetermined streamwise and spanwise spacings. For a smaller streamwise spacing of five roughness heights, the leading roughness elements have little impact on the downstream ones. However, for a larger spacing of ten roughness heights, the wakes of roughness elements influence the downstream ones, inducing different perturbation modes.

The effect of spanwise interaction has drawn relatively less attention. Most of the studies considered a spanwise spacing of more than three times roughness diameter, under which the roughness elements are considered isolated in the array [9,14,21]. Choudhari et al. [22] compared the effect of spanwise wavelength of sinusoidal type of roughness. The decrease of spanwise wavelength leads to a significant reduction in streak amplitude in the wake. Ma and Mahesh [25] reported that smaller spanwise spacing inhibits the formation of counter-rotating vortex pairs and hairpin vortices in the roughness wake. In fact, the spanwise spacing between neighboring elements determines the relative location of the streamwise vortices and velocity streaks [26]. As a result, the downstream roughness elements could locate in either low- or high-speed regions generated by the upstream array depending on the spacing. The growth of velocity streaks and disturbances can be reinforced or canceled by the downstream array. The impact of spanwise spacing on the streaky distribution and characteristics of instability mode needs to be further addressed.

The existing knowledge on roughness induced transition mainly focuses on the zero pressure gradient condition over a flat plate. For engineering airfoil configurations, such as wind/gas turbine blades, the streamline curvature creates pressure gradient, which has been less studied. Stabilization/destabilization of the boundary layer could be produced depending on the localized favorable/adverse pressure gradient [27]. Hack and Zaki [28] studied the effect of adverse pressure gradient on streak instability over a flat plate boundary layer. The ‘inner-mode’ related to the spanwise shear layer between the streamwise velocity streaks is significantly promoted and leads to the breakdown to turbulence. However, with the combined effect of distributed surface roughness configuration and pressure gradient, it is unclear about the distribution and evolution process of the velocity streaks in the roughness wake. The related amplification of disturbance mode and transition onset remains difficult to predict. The former effects will be brought together in the airfoil configuration [5,29–31].

In the present work, we investigate the effects of spanwise and streamwise interactions between roughness elements with canonical distributions. Both single and dual arrays of cylindrical roughness elements are placed on a NACA0012 airfoil. Systematic measurements of the surface temperature and the streamwise velocity component are carried out by using infrared thermography and hotwire anemometry, respectively (Section 2). The number and the spacing of roughness elements in the spanwise direction are varied to investigate their effects on the wake flow topology. A quantitative characterization of the velocity streaks produced by different roughness configurations highlights the correlation between velocity streak distribution, streak amplitude, and transition process; this will be discussed in Section 3 to Section 4. The spectral analysis of velocity fluctuations returns the peak amplitude unstable frequencies (Section 5). The disturbance energy calculated at narrow frequency band reveals two patterns with symmetric and asymmetric spatial distribution. The dominant disturbance type leading to the onset of transition is identified for each roughness configuration.

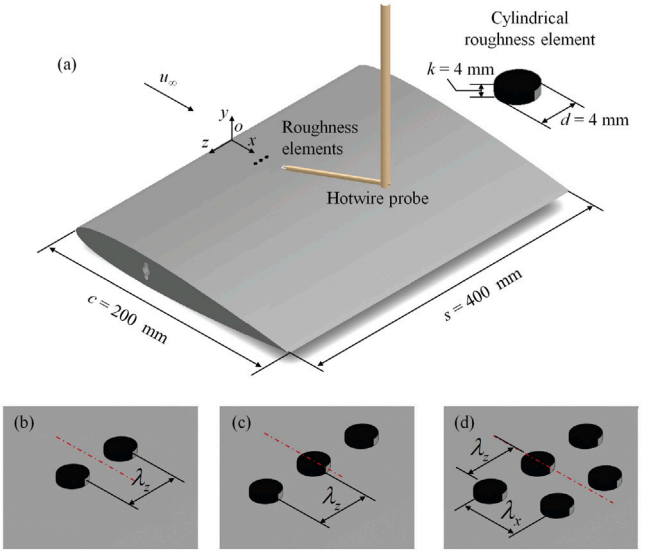

Fig. 1. Sketch of model geometry and installation. (a) Model installation and hotwire setup, (b)–(d) Distribution of roughness arrays, λ_x and λ_z correspond to the streamwise and spanwise spacings between neighboring roughness elements.

2. Experimental setup and measurement techniques

2.1. Flow conditions and test facilities

Experiments were performed in the anechoic open-jet wind tunnel (A-tunnel) of the Aerospace Engineering Faculty at the Delft University of Technology. The wind tunnel has a test section of 0.4×0.7 m^2 with a contraction ratio of 15:1. The maximum operating freestream velocity in this test section is 45 m/s, with a turbulence intensity of less than 0.05% [32]. The freestream velocity distribution across the test section is uniform within 0.5%. A NACA 0012 airfoil of 300 mm chord (c) and 400 mm span (s) (see Fig. 1(a)) was installed at a zero-degree angle of attack. Throughout this paper, we utilize a Cartesian coordinate system (x, y, z) that is centered at the leading edge of the airfoil, such that the x-axis is aligned with the airfoil chord, the z-axis is aligned with the airfoil span, and the y-axis completes the right-handed, orthogonal set of coordinates.

Arrays of cylindrical roughness elements with 4 mm diameter (d) and 1 mm height (k) were placed on one side of the airfoil surface, as shown in Fig. 1(a). The center of the first array of roughness elements was located at $x_r = 0.21c$, which lies downstream of the suction peak at zero degree angle of attack, i.e., within the region of the adverse pressure gradient. The roughness distribution included an isolated element, a spanwise array of elements, and a pair of arrays in stagger, as shown in Fig. 1(b)–(d). Both streamwise and spanwise interactions between neighboring roughness were investigated. The number of elements (N) in the first array includes 2 and 3. The spacing of roughness elements in the spanwise direction is varied from 5 to 12 roughness height (k), as listed in Table 1.

Experiments were performed at a freestream velocity of $u_\infty = 7$ m/s. The corresponding chord Reynolds number ($Re_c = u_\infty c/\nu$) is 1.44×10^5. The Hartree pressure gradient parameter corresponding to the smooth airfoil is defined as:

$$\beta_H = \frac{2\xi}{u_e}\frac{\partial u_e}{\partial \xi}; \quad \xi = \int_0^x u_e(x)dx, \tag{1}$$

where u_e is the velocity at the edge of the boundary layer. At the roughness location $x_r = 0.21c$, β_H is equal to −0.102, confirming the mild adverse pressure gradient condition. The measured boundary layer thickness (δ_{99}), displacement thickness (δ^*), and momentum thickness (θ) at the roughness location are equal to 1.63, 0.58, and 0.22 mm, respectively. The ratio between the roughness height and the boundary layer thickness (k/δ_{99}) is 0.61, indicating that the roughness elements are fully submerged within the boundary layer. The roughness-height-based Reynolds number defined as $Re_{kk} = u_k k/\nu$, is used to estimate the effect of roughness elements on transition. u_k is the velocity at roughness height, and ν is the kinematic viscosity [16]. The correspondent Re_{kk} equals 445 for the current experiment. The critical Re_{kk} scales with the diameter (d) to height (k) ratio of the roughness element, which falls in the range of 140 to 515 for zero pressure condition [33]. Due to the presence of adverse pressure gradient in the current experiment, the threshold of Re_{kk} is expected to be lower than the former range, indicating the supercritical condition.

2.2. Measurement techniques

2.2.1. Infrared thermography

Infrared (IR) thermography measurements were carried out with a CEDIP Titanium 530L IR system. The camera detector has a 320×256 pixels MCT (Mercury cadmium telluride) focal plane array. The spectral response of the sensor falls within the range of 7.7–9.3 μm. The detailed working principle and data processing of the IR camera has been described by Carlomagno and Cardone [34] and Avallone et al. [35]. An objective lens of 25 mm focal length is mounted on the IR camera. The lens aperture is set to $f_\# = 2$. An integration time of 340 μm was used in the experiment to achieve the required signal-to-noise ratio. The recording frame rate was 200 Hz at full resolution. The measurement domain extended from $x/c = 0.1$ until $x/c = 0.7$, resulting in a spatial resolution of approximately 1.74 pixels/mm. The camera was mounted such that the line of sight was along the y axis. In order to increase the temperature difference in presence of the flow, the model surface was heated with two 1 kW halogen lamps. The IR camera is shielded with a foil to avoid heat radiation from the lamp. The IR system was calibrated with a reference black body, accounting for the effects of the viewing inclination of the camera. Spurious contributions due to the ambient radiation were minimized by shielding the camera with a matt-black sheet.

The difference between the measured surface temperature T_s and the spanwise averaged temperature of the undisturbed laminar boundary layer $T_{s,bl}$ is non-dimensionalized by $T_{s,bl}$ as given by,

$$T^* = (T_s(x,z) - T_{s,bl}(x))/T_{s,bl}(x), \tag{2}$$

because the model surface has been preheated, the increased convective heat transfer downstream of transition onset leads to a reduction in the local surface temperature relative to that inside the laminar region. The boundary of the element wake is defined as the outmost spanwise location such that the change rate of surface temperature (Fig. 4), $|\, dT^*/d(z/k)\,|$, is larger than 2.

2.2.2. Hotwire anemometry

The velocity fields behind the roughness elements were measured by hotwire anemometry (HW). A 5 μm diameter single-wire probe (Dantec Dynamics P11) was operated by a constant temperature bridge (TSI IFA-300) with an automatic overheat ratio adjustment. The development of the roughness wake is captured at five $y-z$ cross-planes behind the roughness elements. The cross-plane locations for all roughness distributions are summarized in Table 1. The sketch of the HW setup is shown in Fig. 1. The movement of the hotwire probe is controlled by a computer-controlled traverse system with three degrees of freedom. The spatial resolution of the traverse system in all three directions is less than 2 μm. For each cross-plane, the boundary layer profile consists of 30 measurement points in the wall-normal direction to resolve the wall shear layer. The wall-normal spacing between neighboring points changes from 0.02 mm, 0.04 mm, 0.1 mm, 0.15 mm, 0.2 mm from the wall to the freestream, providing higher spatial resolution in the near wall region. The boundary layer profiles are measured with equal spacing of 1 mm in the spanwise direction. The number of measurement

Table 1
Roughness element distributions and HW measurement planes downstream of the roughness elements, x_r denotes the center of the roughness elements within the upstream array.

Distribution	Number of elements in the first array (N)	$\lambda_z/k = \lambda_x/k$	HW planes $x_s/k = (x - x_r)/k$
Isolated cylinder	1	–	6, 15, 32, 46, 80
Single array	2	12, 8, 6, 5	6, 15, 32, 46, 80
Single array	3	8, 6	6, 15, 32, 46, 80
Dual arrays	2 or 3	8	14, 23, 40, 54, 88
Dual arrays	2 or 3	6	12, 21, 38, 52, 86

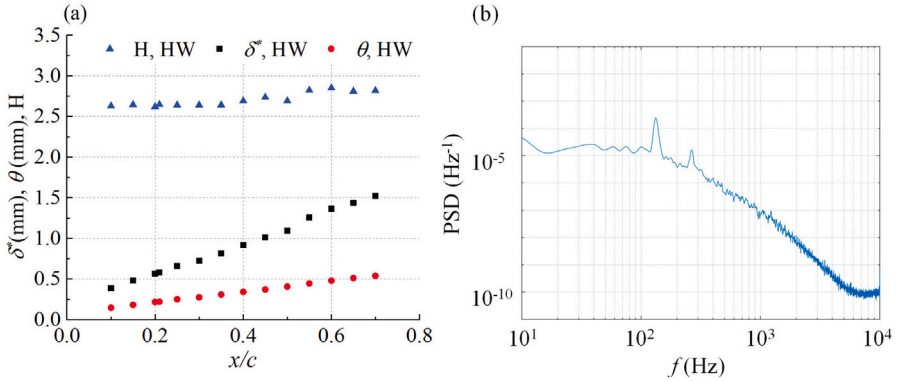

Fig. 2. Boundary layer properties on the NACA0012 airfoil, (a) HW measurement over the whole domain, (b) PSD of streamwise velocity fluctuations at $x/c = 0.95$.

locations in the spanwise direction depends on the roughness configuration, providing full coverage of the roughness wake. The measurement data were acquired at a sampling frequency of 50 kHz with a low-pass filter with a cut-off frequency of 20 kHz. The measurement period at each point is 2 s, ensuring an adequate statistical convergence. With a typical level of streamwise velocity fluctuations of $u'/u_\infty = 0.1$, the uncertainty of the time-averaged streamwise velocity (ϵ_u) and RMS of streamwise velocity fluctuations (ϵ_{rms}) are $0.032\%u_\infty$ and $0.023\%u_\infty$, respectively [16].

2.3. Undisturbed laminar boundary layer

Boundary layer profiles for the clean airfoil configuration (i.e., without any roughness elements) were measured at the freestream velocity of 7 m/s at selected locations of the airfoil. The development of the displacement thickness (δ^*), momentum thickness (θ), and shape factor ($H = \delta^*/\theta$) over the entire streamwise extent of the measurement domain are shown in Fig. 2(a). The boundary layer shape factor within this region approximately corresponds to H = [2.6, 2.8], indicating the laminar condition of the undisturbed boundary layer. The shape factor increases from upstream to downstream due to the effect of the adverse pressure gradient. The onset of transition is detected at $x/c = 0.95$ by the decrease of surface temperature due to the higher convective heat transfer. The power spectral density (PSD) of streamwise velocity fluctuations ($\langle u' \rangle_{rms}/u_\infty$) at the transition location (Fig. 2(b)) is centered at a fundamental frequency of 130 Hz and the first harmonic, corresponding to the peak frequency of the TS wave amplification [36].

3. Time-averaged wake flow topology and velocity fluctuations

3.1. Isolated cylinder

The flow topology around and downstream of an isolated cylindrical roughness element is first analyzed as a baseline. The surface signature of the near-wall flow features is shown by the non-dimensional surface temperature distribution T^* in Fig. 3, where $x_s = x - x_r$. Similar to the prior measurements under zero pressure gradient [37], the flow separates a short distance upstream of the cylinder, forming a system of horseshoe vortices within the region of upstream separation. These spanwise vortices produce high values of shear stress in the close vicinity of the cylinder, accompanied by higher values of surface heat transfer (dark gray, see Fig. 3). The horseshoe vortices wrap around the upstream face of the cylinder and realign with the streamwise direction within the cylinder wake, leading to the generation of low- and high-speed velocity streaks. The flow features show topological similarity between the current experiment under adverse pressure gradient and previous research under zero-pressure gradient condition [8,17,38].

The momentum transport in the cylinder wake is quantitatively investigated by the difference between time-averaged streamwise velocity (u/u_∞) and the undisturbed boundary layer (u_{bl}/u_∞), as $u_d/u_\infty = (u\text{-}u_{bl})/u_\infty$. The cross-plane contours of velocity difference are shown at selected streamwise locations (x_s/k = 6, 15, 32, 46 and 80) in Fig. 3 with contour lines of u/u_∞ superimposed. The negative and positive values of u_d correspond to the velocity deficit and excess, shown as blue and red regions in the contours. Close to the cylinder at $x_s/k = 6$, the streamwise vortices originating from the horseshoe-vortex system induce lateral upwash motion at $z/k = \pm 3$, generating two low-speed regions (referred to as 'SL') [13,17]. These vortices transport high-momentum fluid toward the wall near the symmetry plane, leading to the formation of high-speed regions at $z/k = \pm 2$ and low-temperature streaks. Moreover, a central region of low-speed flow (referred to as 'CL') forms due to the flow separation behind the cylinder. The inflectional velocity profile produced by the former low-speed regions is prone to the growth of Kelvin–Helmholtz (K–H) instability and the production of strong velocity fluctuations [9,16]. Moving downstream ($x_s/k > 6$), the velocity deficit in the CL region is reduced considerably as the flow recovers from separation behind the roughness element due to viscous diffusion [13]. In contrast, the horseshoe vortices sustain the momentum transport and high magnitude velocity difference within the SLs. The additional streamwise vortices and the induced high-speed regions form at the spanwise sides, as shown by the outer secondary low-temperature regions in Fig. 3. The spanwise locations of the streamwise vortices remain nearly constant until the end of the IR measurement domain. As a result, the wake of the isolated cylinder sustains a laminar condition in the measurement domain of interest.

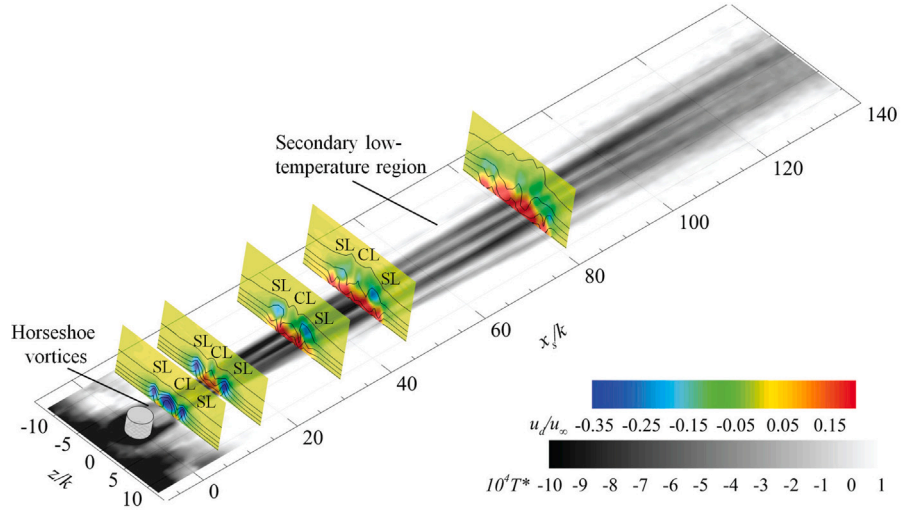

Fig. 3. Flow topology around and downstream of isolated cylinder. Surface temperature distribution (T^*) and cross-plane contours of streamwise velocity difference (u_d/u_∞) are visualized. The contour lines of non-dimensional time-averaged velocity (u/u_∞) with an increment of 0.1 are superimposed. Distances along the y axis are magnified by a factor of 3 for better visualization.

3.2. Spanwise interaction of cylinders in an array

When roughness elements are placed with close spanwise intervals, the interaction between neighboring counter-rotating streamwise vortices could lead to significant reinforcement of velocity streak amplitude and regeneration of new streaks, associated with the onset of transition. The investigation of the spanwise interaction between multiple roughness elements starts with the configurations with 2 and 3 cylinders in a single array. These are designed to investigate the effect of an even and odd number of elements [22,39]. Different spanwise spacings are investigated to address the effect of λ_z/k on wake flow topology, growth of disturbances and transition onset.

3.2.1. Two cylinders in the array

Pairs of cylinders with decreasing spanwise spacing of λ_z/k = 12, 8, 6 and 5 were tested. The surface temperature distribution behind the array of two cylinders is shown in Fig. 4. For the largest spanwise spacing λ_z/k = 12 (Fig. 4(a)), two separate wake regions are present behind each roughness element. Each wake shows similar streak structures and velocity deficit as those described earlier for the isolated cylinder, indicating weak interaction between neighboring elements [9,14]. At smaller spanwise spacings (Fig. 4(b)–(d)), the wakes start to connect and become fully merged when evolving downstream. The onset of spanwise wake interaction moves gradually upstream with decreasing spanwise spacing, occurring close to or even at the roughness location. We now examine the distributions of the streamwise velocity difference (u_d/u_∞) and the RMS of the streamwise velocity fluctuations ($\langle u' \rangle_{rms}/u_\infty$) for the cases with median spanwise spacings, namely λ_z/k = 8 and 6. The former configurations correspond to the condition when the roughness wake starts to interact and fully merged. The cross-plane contours of these two quantities at four selected streamwise locations (x_s/k = 6, 15, 32, and 80) are shown in Fig. 5 and 6 for decreasing values of λ_z/k.

For the spanwise spacing λ_z/k = 8, the interaction between the wakes of each cylinder emerges at the most upstream measurement station x_s/k = 6 (Fig. 5(a.1)). The interference features as a connection between the respective SLs close to z/k = 0. The maxima of velocity fluctuations remain concentrated at the CLs (Fig. 5(b.1)). Moving downstream, the continued spanwise propagation of each wake toward z/k = 0 leads to a complete merger of the SLs to form a single low-speed region (referred to as 'merged low-speed region (MLS)') at x_s/k = 15 (Fig. 5(a.2)), leading to higher velocity deficit ($u_{d,min}/u_\infty$ = −0.64) than that produced at the same streamwise location for the isolated cylinder. The growth of $\langle u' \rangle_{rms}/u_\infty$ around the MLS is observed (Fig. 5(b.2)). Further downstream at x_s/k = 32 (Fig. 5(a.3)), the MLS lifts up from y/k = 1 to y/k = 2 as a result of the upwash motion produced by counter-rotating streamwise vortex pair [16]. The velocity deficit of this MLS reduces at this stage. Similarly, Ye et al. [17] observed that the streamwise evolution of the maximum velocity deficit follows a power-law type decay. However, a higher level of velocity fluctuations is obtained at the wall-normal and spanwise shear layers of the MLS in comparison with the fluctuation levels within the CLs and the SLs (see Fig. 5(b.3)), indicating the importance of MLS on the growth of disturbances [9,37]. At x_s/k = 80 (Fig. 5(a.4)), the CLs and the MLS fully merge into one single low-speed region close to the center plane with more uniform distribution of the velocity fluctuations (Fig. 5(b.4)), further sustaining the amplitude of the merger and its dominance on the perturbation growth.

For lower spanwise spacings λ_z/k = 6, the evolution process of velocity streaks is accelerated. The SLs of each cylinder wake form at the identical spanwise location of z/k = 0, promoting a complete merger right behind the cylinders at x_s/k = 6 (Fig. 6(a.1)). The velocity deficit further increases to $u_{d,min}/u_\infty$ = −0.72 with respect to that for the configurations with larger spanwise spacing. At the downstream measurement stations (Fig. 6(a.2)–(a.3)), the MLS undergoes a faster lift-up process under the effects of a stronger low-speed region and stronger upwash motion. The CLs behind each cylinder quickly merge with the MLS, pertaining a large velocity deficit until the farthest downstream measurement station at x_s/k = 80 (Fig. 6(a.4)). The high-intensity MLS and the associated inflectional velocity profile feed the growth of the instability waves (Fig. 6(b.4)), resulting in a significantly higher level of velocity fluctuations at the surrounding shear layer than that of the λ_z/k = 8 case. Away from the center region, one observes two maxima in the velocity fluctuation amplitude at the SLs on either side for x_s/k = 80 (Fig. 6(a.4)), contributing to the lateral growth of the unsteady disturbances and onset of turbulent wedge [17,40,41]. The merging process from isolated roughness wakes into a single wake is similar to that observed downstream of circular cylinder patches submerged in the turbulent boundary layer [42,43] and two parallel jets [44].

To quantify the effect of spanwise spacing on transition onset, the streamwise evolution of the wake width is characterized in Fig. 7, being extracted from the surface temperature distribution (see Section 2.2.1). The y axis is the overall wake width subtracted by the spanwise spacing of the cylinders (w/k – (N-1)λ_z/k) for better visualization of the wake spreading. The transition onset location is defined as the streamwise

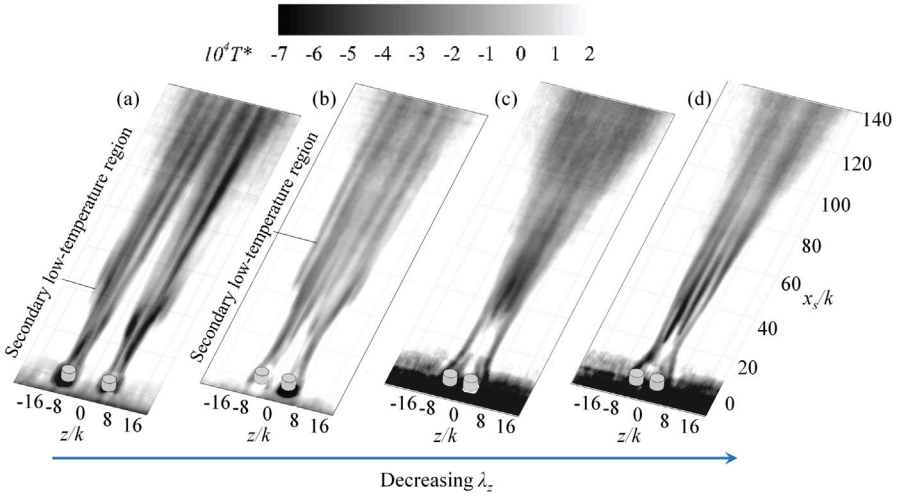

Fig. 4. Surface temperature distribution (T^*) behind a single array with two cylinders, (a)–(d) correspond to λ_z/k = 12, 8, 6 and 5, respectively.

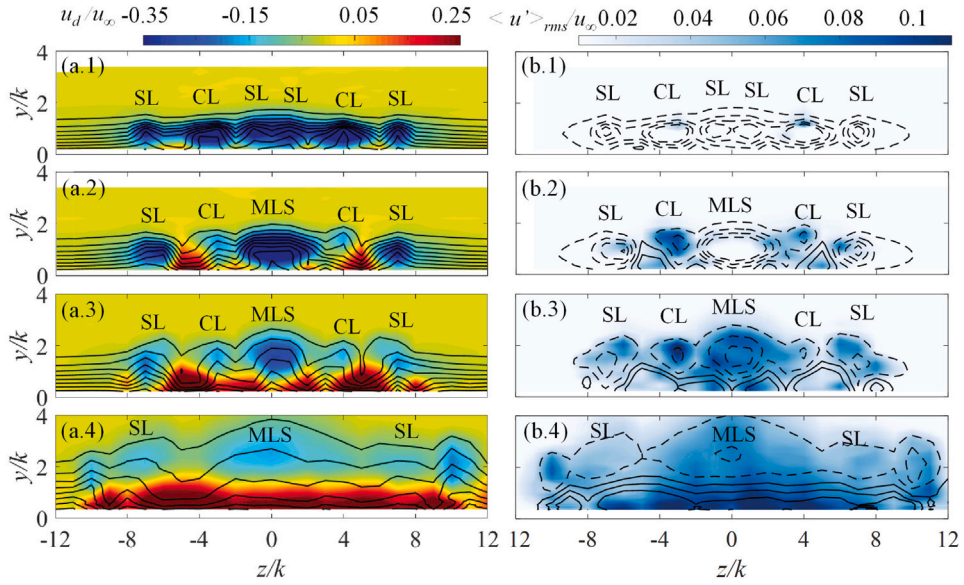

Fig. 5. Cross-plane contours of (a) streamwise velocity difference (u_d/u_∞) and (b) streamwise velocity fluctuations ($\langle u' \rangle_{rms}/u_\infty$) in the wake of a single array of two cylinders with λ_z/k = 8. Contour lines of u/u_∞ and u_d/u_∞ are superimposed in (a) and (b), respectively. The solid and dashed lines correspond to the positive and negative value, respectively. (1)–(4): x_s/k = 6, 15, 32, and 80. MLS, CL, and SL indicate merged, central, and sideward regions of low-speed flow.

location where the spanwise width of the wake starts increasing, indicating the formation of a turbulent wedge [45]. The former locations are highlighted by the red dots in the plot. The lateral growth in wake width can only be observed for the two smallest spanwise spacings of λ_z/k = 6 and λ_z/k = 5 (Fig. 7), starting from x_s/k = 63 and x_s/k = 71, respectively, corresponding to the transition locations. For these cases, the neighboring sideward low-speed regions undergo an early merging. The high-velocity deficit produced at the merged low-speed region appears to induce an inflectional instability at the surrounding shear layer and a large enough disturbance growth, which is believed to induce transition to turbulence. For the larger spanwise spacings of λ_z/k = 12 and λ_z/k = 8, the wake width remains constant in the downstream region, implying a laminar condition throughout the measurement region. The transition locations for all the cases are summarized in Table 2.

3.2.2. Three cylinders in the array

Increasing the number of roughness elements in the array introduces additional flow structures in the wake, which further modifies the velocity streak distribution and adds extra complexity to the wake interaction [46]. In this section, the effect of the number of roughness elements on the transition process is investigated by placing three cylindrical roughness elements in an array with spanwise intervals (λ_z/k) equal to 8 and 6. As shown by the surface temperature distribution in Fig. 8, the overall flow patterns and the presence of additional flow structures reveal a more notable dependence on spanwise interval. The cross-plane contours of the streamwise velocity fluctuations ($\langle u' \rangle_{rms}/u_\infty$) for λ_z/k = 8 and λ_z/k = 6 are detailed in Fig. 9 at x_s/k = 15, 32, and 80. The velocity streaks are visualized by the superimposed contour lines of u_d/u_∞, with solid and dashed lines representing the positive and negative values, respectively. Similar to the case of an array with two cylinders, the neighboring sideward low-speed regions (SL) behind the three-cylinder array connect and form merged low-speed regions (MLS) on both sides of the middle cylinder (Fig. 9(a.1)(b.1)).

For λ_z/k = 8 (Fig. 9(a)), the two MLS persist downstream at a nearly constant spanwise position. The CLs do not fully merge with the MLSs until x_s/k = 80. The velocity fluctuations around the CLs, the

Table 2
Transition onset locations. Key for case designation: N: number of cylinders in the first array. The last column is the spanwise interval (λ_z).

Roughness distribution	Transition onset (x_s/k)	$A_{u,max}$	Roughness distribution	Transition onset (x_s/k)	$A_{u,max}$
Isolated cylinder	–	0.34	Single–N3–8k	123	0.43
Single–N2–12k	–	0.36	Single–N3–6k	82	0.54
Single–N2–8k	–	0.41	Dual–N2–8k	80	0.46
Single–N2–6k	63	0.50	Dual–N2–6k	74	0.50
Single–N2–5k	71	0.48	Dual–N3–8k	92	0.45
			Dual–N3–6k	78	0.49

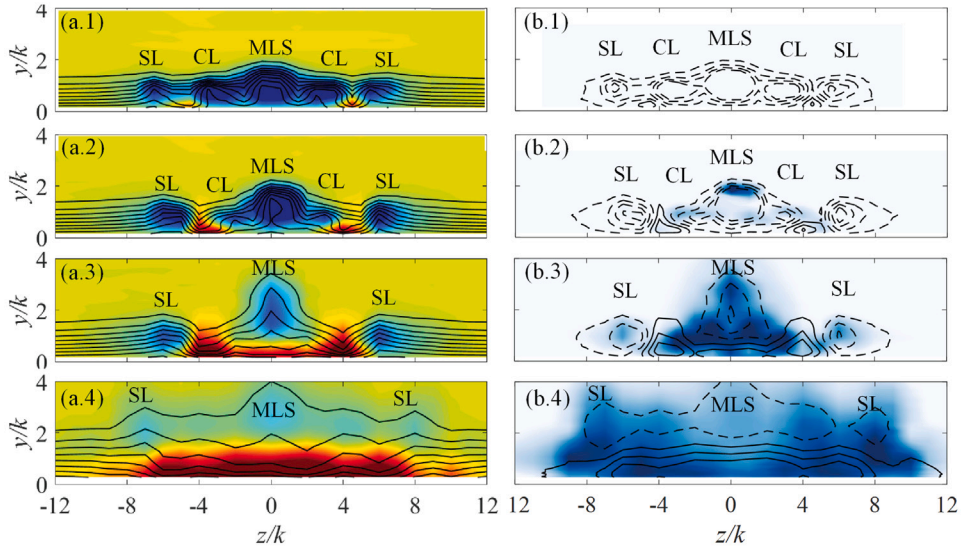

Fig. 6. Cross-plane contours of (a) u_d/u_∞ and (b) $\langle u' \rangle_{rms}/u_\infty$ in the wake of a single array of two cylinders with $\lambda_z/k = 6$. The detailed description can be found in Fig. 5.

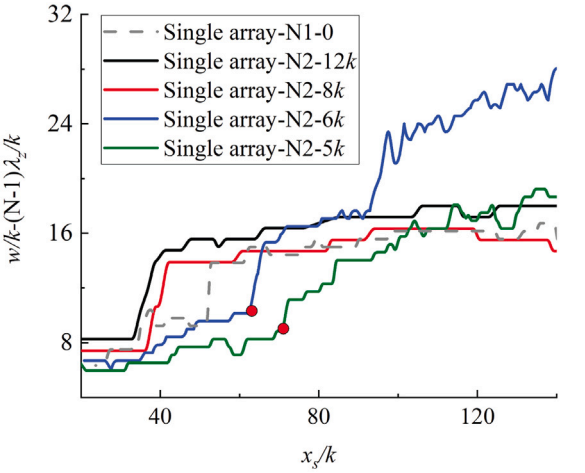

Fig. 7. Streamwise evolution of wake width (w/k) behind a single array with two cylinders. N: number of cylinders in the array. (N-1)λ_z/k is subtracted for ease of comparison. The last column of the legend denotes the spanwise spacing (λ_z). The red dots indicate the transition onset location.

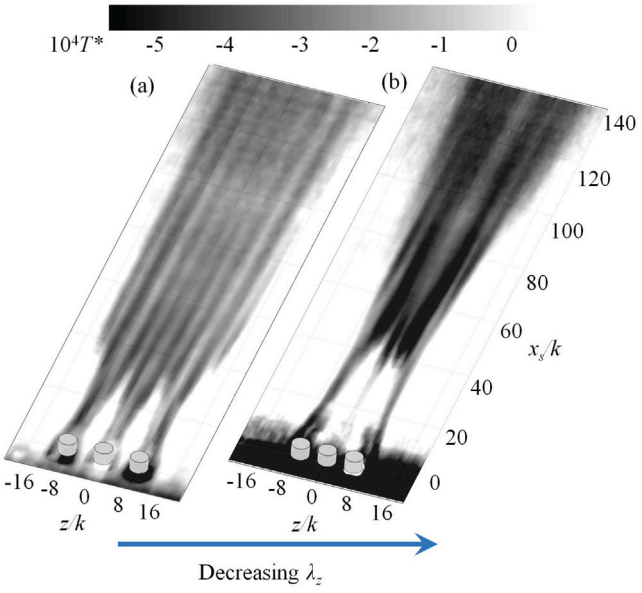

Fig. 8. Surface temperature distribution (T^*) behind a single array with three cylinders. (a) and (b) correspond to $\lambda_z/k = 8$ and 6.

SLs, and the MLSs exhibit similar level of intensity when $x_s/k \geq 32$ (Fig. 9(a.2)–(a.3)), weakening the dominance of MLS in the growth of disturbances observed in the dual cylinder case. Besides the local K-H instability induced by each MLS, the coexistence and the interaction of the two MLSs lead to the growth of asymmetric mode beneath the wall-normal shear layer [46,47], accelerating the overall growth of unsteady disturbances. The scenario agrees with the bypass transition process under adverse pressure gradient, promoting the growth of near-wall sinuous disturbances [28]. A detailed analysis of the disturbance growth is presented in Section 5.

For the smaller spanwise spacing of $\lambda_z/k = 6$ (Fig. 9), the MLS evolution follows a different pattern. Instead of remaining at a nearly constant spanwise location observed in the $\lambda_z/k = 8$ case, the two

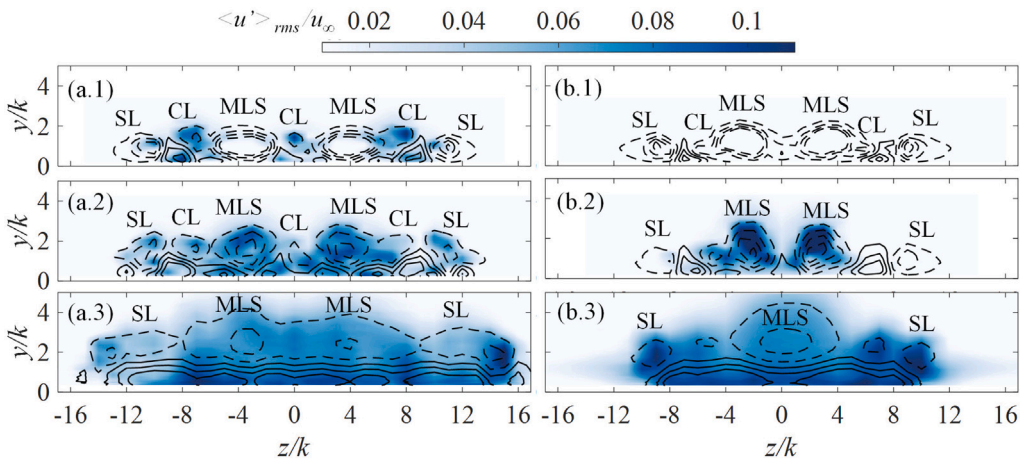

Fig. 9. Cross-plane contours of streamwise velocity fluctuations ($\langle u' \rangle / u_\infty$) in the wake of a single array of three cylinders, (a) λ_z/k = 8, (b) λ_z/k = 6. Contourlines of u_d/u_∞ is superimposed. The solid and dashed contour lines correspond to the positive and negative values of u_d/u_∞, respectively. Parts (1)–(3) in each subfigure correspond to x_s/k = 15, 32, and 80. MLS, CL, and SL indicate merged, central, and sideward regions of low-speed flow.

MLSs now move toward the symmetry plane as x_s/k increases (Fig. 9(b.1)–(b.3)). The growth of velocity fluctuations is significantly delayed in comparison with two cylinder configuration (Fig. 6(b)), possibly due to the interaction between the MLSs. The first appearance of high-intensity fluctuations of streamwise velocity is postponed to x_s/k = 32 (Fig. 9(b.2)), specifically around the shear layer of the MLSs. The overall intensity of velocity fluctuations is remarkably lower than that of the double cylinder case, retarding the spanwise propagation of the disturbances and onset of transition. At x_s/k = 80 (Fig. 9(b.3)), the MLSs fully merge into one single low-speed blob, yielding a similar symmetric velocity streak distribution to the two cylinder array.

From the distribution of velocity fluctuations, it is conjectured that the disturbance growth is related to asymmetric and symmetric types of instability for λ_z/k = 8 and 6, respectively, indicating different transition mechanisms. Considering the transition onset, the surface temperature distribution (T^*) in Fig. 8 shows the wake spreading at x_s/k = 120 and 82 for case λ_z/k = 8 and 6, respectively. Compared with the dual cylinder array (see Table 2), the effect of additional roughness on transition onset depends on the spanwise spacing, which anticipates and delays for the case λ_z/k = 8 and 6, respectively.

3.3. Streamwise interactions of dual arrays with staggered distributions

To analyze the effects of the streamwise interaction on the overall flow topology as well as the transition process, two arrays of the cylindrical roughness elements are arranged in a staggered distribution with equal streamwise (λ_x) and spanwise (λ_z) spacings of 8k. The configuration with three cylinders in the upstream array and two cylinders at the downstream station is examined (Fig. 1(d)). The second rows of roughness are placed in the low-speed region produced by the upstream row before the streak magnitude reaches the maximum. The wake flow is inspected using the contours of the RMS of streamwise velocity fluctuations ($\langle u' \rangle_{rms}/u_\infty$) as shown in Fig. 10(a) at three streamwise stations ($x_{s,2}/k = x_s/k - \lambda_x/k$ = [15, 46, and 80]). The contour lines of streamwise velocity difference (u_d/u_∞) are superimposed.

The detached shear layer induced by the first cylinder array interacts and merges with the shear layer generated by the second array [21,48], leading to the enhancement of the velocity deficit and the local shear stress at the MLSs in the near wake. The second array counteracts with the CLs produced by the upstream array, which are pushed away from the center plane, separating from the MLSs throughout the wake. The counteraction reduces the streamwise velocity fluctuations around the CLs and SLs at the spanwise sides for $x_{s,2}/k$ = 15 (Fig. 10(a.1)) in comparison with the single array case. On the other hand, the unstable shear layer around MLSs with augmented velocity deficit supports the continuous perturbation growth when moving downstream ($x_{s,2}/k$ = 46, Fig. 10(a.2)), leading to a higher level of velocity fluctuations. This suggests that the new low-speed region, generated by the second array, pertains the strength of MLS before the decaying process, which anticipates transition. One could note that at $x_{s,2}/k$ = 46, the distribution of velocity streak and velocity fluctuations lose their spanwise symmetry, enhancing the differences of the velocity fluctuations between the $z > 0$ and $z < 0$ sides. The two MLSs remain separated all the way until the last measurement station of $x_{s,2}/k$ = 80 (Fig. 10(a.3)), where the cross-plane distribution of velocity fluctuations is seen to be nearly homogeneous with high intensity of 0.1. As a result, one would expect that the transition process is induced via the same instability mechanism as the single array cases.

The presence of the notable asymmetry for this configuration in the vicinity of $z = 0$ is also observed from the surface temperature distribution in Fig. 10(b). The curved low-temperature streak corresponds to the high-speed regions formed between the MLSs. The spatially meandering streak path is attributed to the spanwise interaction between the two MLSs, indicating a possible growth of the asymmetric type of disturbance mode, which dominates the process toward transition [46]. The former region can be clearly detected all the way from the near wake up to x_s/k = 108, which is downstream of the inception of the turbulent wedge at x_s/k = 92, yielding a significant earlier onset of transition than the single array case (Fig. 8).

4. Streamwise evolution of streak amplitude

As seen in the previous sections, the distribution and spacing of roughness elements influence the magnitude of low- and high-speed regions, resulting in different growth rates of unsteady disturbances and transition onset locations. The amplitude of the spanwise modulation caused by the presence of the roughness elements can be characterized via the streak amplitude (A_u), defined as:

$$A_u(x) = \frac{1}{2}[\max_{y,z}(u_d(x,y,z)/u_\infty) - \min_{y,z}(u_d(x,y,z)/u_\infty)], \quad (3)$$

The above definition of streak amplitude was proposed by Andersson et al. [49] for the study of bypass transition and it has been widely used in other studies of roughness element wakes [26,50]. The augmentation of A_u is favorable for the growth of both the K-H and the asymmetric instabilities [2]. These instability modes contribute to the enhancement of streamwise velocity fluctuations. For an isolated cylinder ('N1-0' in Fig. 11(a)), the maximum value of A_u is 0.34. The variation in the streak amplitude across the various measurement stations is relatively

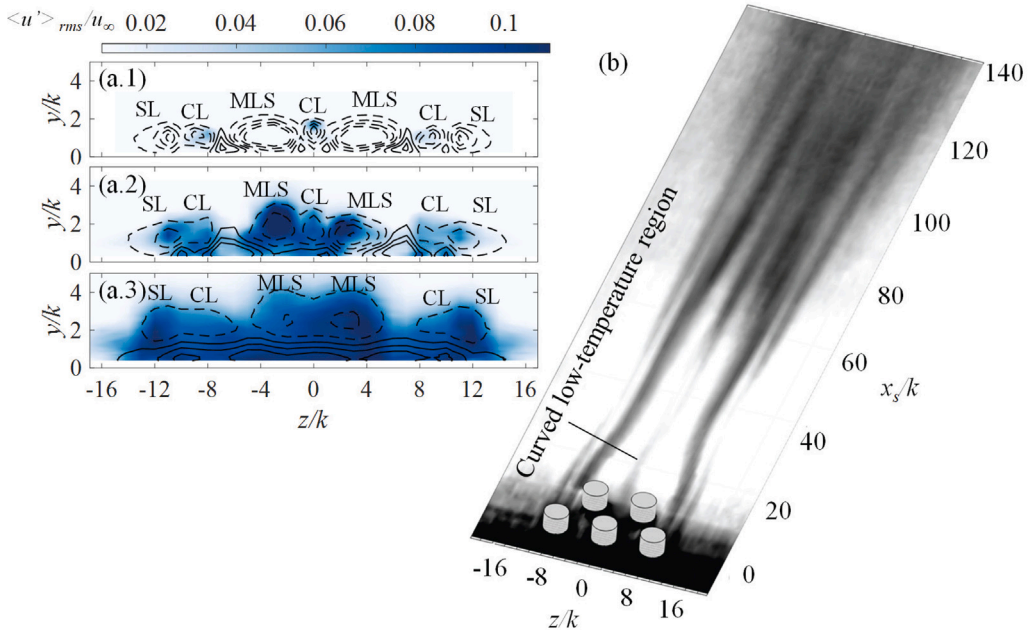

Fig. 10. Flow topology around and downstream of dual cylinder arrays. Three cylinders are placed in the first array with $\lambda_z/k = 8$. (a) Cross-plane contours of streamwise velocity fluctuations ($\langle u' \rangle_{rms}/u_\infty$), with the contour lines of u_d/u_∞ being superimposed. (1)–(3) correspond to $x_{s,2}/k$ = [15, 46, and 80]. CL, SL, and MLS indicate the low-speed regions. (b) Surface temperature distribution (T^*).

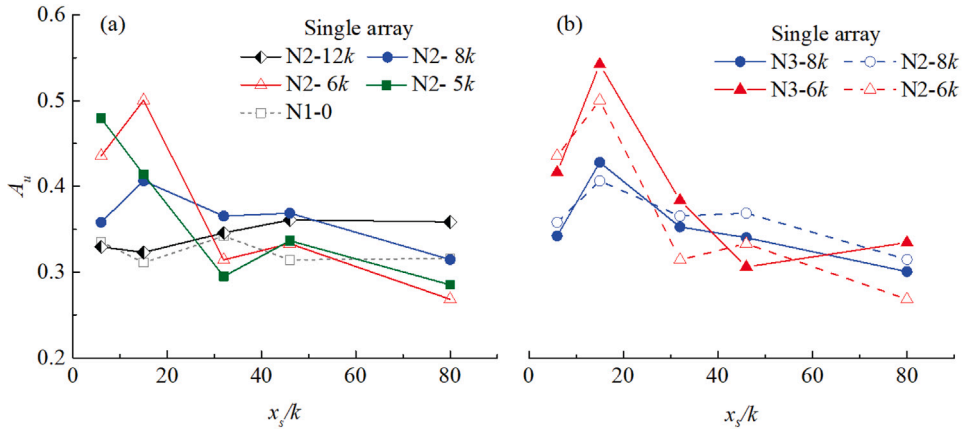

Fig. 11. Streak amplitude (A_u) behind an isolated cylinder and a single array of two (a) and three (b) cylinders. N: number of cylinders in the first array. The last part of the legend name is the spanwise interval (λ_z).

small. Fransson and Talamelli [26] found similar streak amplitude produced by an array of roughness elements, without inducing secondary instability and transition.

The spanwise interaction between roughness elements in the array influences both the peak amplitude and location. In the case of an array of two roughness elements, the decrease of spanwise interval leads to the growth of streak amplitude and upstream movement of the peak location. The variation of A_u arises when $\lambda_z/k = 8$ (N2-8k) and becomes remarkable for $\lambda_z/k = 6$ and 5 (case N2-6k and N2-5k in Fig. 11(a), respectively). The earlier inception of the merged low-speed region leads to faster growth in A_u, yielding higher peak amplitudes of $A_{u,max} = 0.50$ and $A_{u,max} = 0.48$ for $\lambda_z/k = 6$ and 5, respectively. For both cases, the peak amplitude is reached farther upstream at $x_s/k = 15$ and 6, after which the streak amplitude decreases sharply being attributed to a more pronounced spanwise mixing and wake recovery. Note that the growth of the peak streak amplitude is not monotonic with decreasing λ_z. The largest peak is achieved when the SLs fully overlap for the condition $\lambda_z/k = 6$, as shown in Fig. 6. As been found by Choudhari et al. [22], further decrease in spanwise spacing leads to a strong reduction in peak streak amplitude.

When the number of roughness elements in the array is increased for the $\lambda_z/k = 8$ and $\lambda_z/k = 6$ cases (case N3-8k and N3-6k, Fig. 11(b)), the streak amplitude evolution follows similar trends as the array with two cylinders but reaches a higher magnitude at the intermediate measurement stations. However, the transition onset location is anticipated for the $\lambda_z/k = 8$ case and delayed for the $\lambda_z/k = 6$ case, revealing the dependence on spanwise spacing and the change of dominant instability mode leading to transition.

For the configurations with dual arrays (Fig. 12), the regeneration of low-speed regions by the second array influences the evolution of streak amplitude. A_u rises significantly in the near wake in comparison with the single array case for the larger spanwise interval of $\lambda_z/k = 8$, due to the reinforcement of merged low-speed regions by the downstream array [2,21,26]. The augmentation of A_u is favorable for the growth of streamwise velocity fluctuations, which in turn can lead to an earlier transition than the single-array case (see Table 2). On the other hand, for the smaller spanwise interval of $\lambda_z/k = 6$ (Fig. 12), the A_u obtained

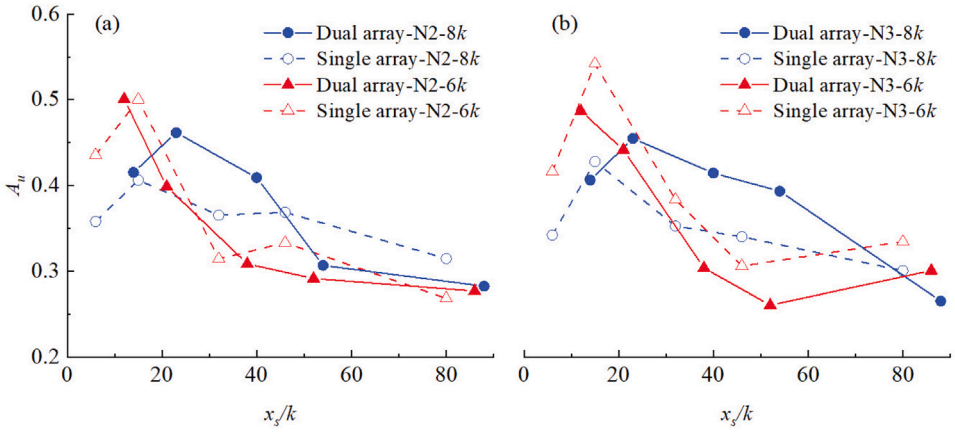

Fig. 12. Streak amplitude (A_u) evolution behind single and dual arrays of cylinders, (a) with two and (b) three elements in the first array. The details can be found in Fig. 11.

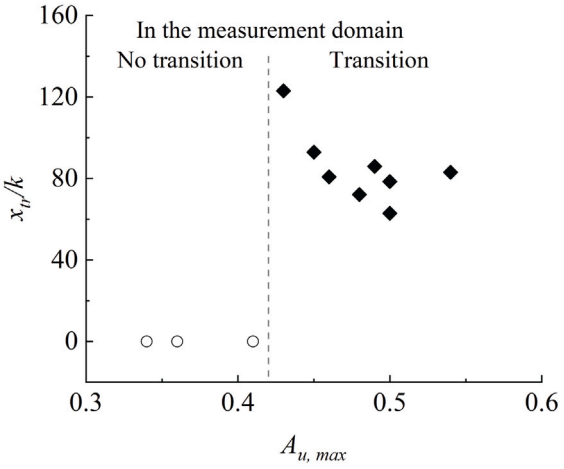

Fig. 13. Transition location against $A_{u,max}$ for all roughness distributions.

for the dual array configuration reaches the maximum at the most upstream station, which follows by a fast decaying process due to the cancellation effect for CL and SL by the downstream array. As a result, A_u is similar to or even slightly lower than that behind the single array when $x_s > 15$ [24]. Consequently, transition is delayed downstream. A similar dependence of streak amplitudes on streamwise separation has been noted for roughness elements arranged in tandem at a single spanwise location was obtained by Choudhari et al. [2] and Chou et al. [51]. They proposed that the larger streamwise spacing leads to higher streak amplitude. However, the effect of streamwise separation in the context of staggered spanwise arrangements of roughness elements has been characterized here for the first time.

The transition locations (x_{tr}) for the various roughness configurations are plotted against the maximum value of A_u in Fig. 13. The onset of transition is observed when $A_{u,max} > 0.42$, providing an approximate correlation between the streak amplitude induced by the roughness elements and a sufficiently large growth of instability waves to induce transition [52–54]. The critical streak amplitude is also in agreement with that produced by Shahinfar et al. [55] in the low turbulence wind tunnel. The transition locations based on the inception of wake width increase and the maximum A_u for all of the cases are summarized in Table 2. When the streak amplitude behind an array is smaller than the critical value (e.g., $A_u < 0.42$ for both $\lambda_z/k = 12$ and 8), the amplitude of the velocity fluctuations in the array wake is comparable to those in the case of an isolated roughness element, wherein transition did not occur within the measurement domain. The earliest transition occurs for the intermediate spanwise spacing of $\lambda_z/k = 6$ wherein a higher $A_{u,max}$ is obtained due to the perfect overlap between the neighboring sideward low-speed regions (see Fig. 6). Although the streamwise evolution of A_u cannot be fully described and the exact critical value of $A_{u,max}$ cannot be obtained in the current paper due to the limited number of measurement stations, it is reasonable to conjecture that an optimal spanwise spacing (λ_z) to promote transition corresponds to that for which the spanwise interaction between the roughness elements leads to the maximum peak amplitude of the velocity streaks.

5. Spectral analysis for single roughness array

The streamwise velocity fluctuations associated with the most energetic instability modes in the roughness wake correspond to either a symmetric or an asymmetric distribution along the spanwise direction [49,50]. The spanwise and streamwise interactions between the wakes of the roughness elements play a key role in streaky flow modulation, determining which of these two modes dominates the disturbance growth within the wake. To investigate the influence of roughness distribution on the frequency and the spatial pattern of the dominant instability mode in the wake, we next analyze the power spectral density (PSD) of non-dimensionalized streamwise velocity fluctuations ($\langle u' \rangle / u_\infty$). The PSD at the inflection points of the wall-normal shear layer (i.e., where $\partial u/\partial y$ reaches a maximum) around the low-speed regions are compared between the isolated cylinder case, and the single array configurations with two and three cylinders with spanwise spacing of $\lambda_z/k = 8$ and $\lambda_z/k = 6$. The PSD for the undisturbed boundary layer at the roughness height is also plotted for comparison. The results for dual array configurations are not detailed here for conciseness, as the flow pattern and the instability mechanism are the same as those of the single array configuration (see Section 3.3).

5.1. Isolated cylinder

The frequency spectra at selected locations across the cross-section of the wake behind an isolated cylinder are plotted in Fig. 14 for the streamwise locations of $x_s/k = 6$. A dominant peak at $f_{c,0} = 1080$ Hz that achieves its largest amplitude at the inflection point of the CL is observed. This spectral peak is associated with the shedding frequency of the hairpin vortices behind the roughness elements [37,56]. The corresponding Strouhal number ($St = fk/u_\infty$) equals 0.15, which is similar to that obtained by White and Ergin [57] and Choudhari and Fischer [14] for a cylindrical roughness element with an aspect ratio (d/k) of 5.6. Three additional low-frequency peaks in the spectra can be noted at 30 Hz, 50 Hz, and 170 Hz, respectively. Contours of band-pass filtered streamwise velocity fluctuations at 30 Hz and 50 Hz exhibit maxima within the spanwise shear layer of the CL (not shown

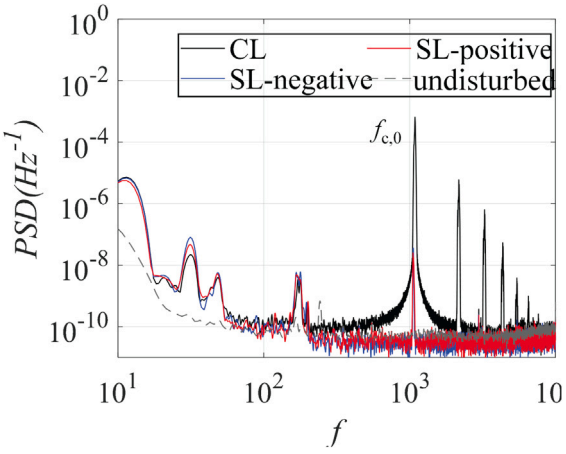

Fig. 14. Power spectral density at the inflection points at the wall-normal shear layer of the different low-speed regions for isolated roughness element at $x_s/k = 6$. CL and SL indicate central and sideward low-speed regions.

here for the sake of conciseness), indicating the emergence of a weak asymmetric instability [13,58]. For the peak at 170 Hz, the highest intensity fluctuations appear at the wall-normal shear layer of both the CL and the SLs. This low-frequency peak is close to the TS wave frequency of the undisturbed boundary layer (see Fig. 2(b)), indicating the amplification of freestream disturbances by the cylinder [59].

5.2. Single array with two cylinders

For a single array of two cylinders, PSD analysis is performed at $x_s/k = 32$, where high-level velocity fluctuations begin to emerge (see Figs. 5 and 6). For $\lambda_z/k = 8$ (Fig. 15(a)), the PSDs at the inflection points of the MLS exhibit a broadband amplitude increase with respect to the PSD of the undisturbed boundary layer. The peak at $f_{c,0} = 1000$ Hz, and its harmonics exhibit the highest PSD amplitude (Fig. 15(a)). This frequency is similar to the shedding frequency of the hairpin vortices found for the isolated cylinder. In other words, the dominant frequency appears to be relatively insensitive to the proximity of the other roughness elements within the array. Additional peaks with fundamental frequency at $f_{L,1} = 30$ Hz and its harmonics are also observed, being associated with the velocity fluctuations at the spanwise shear layer.

To detect the instability mechanisms associated with each frequency peak, the unsteady disturbance energy is calculated over a narrow frequency band as:

$$e_f(x, y, z) = \int_{f-\Delta f}^{f+\Delta f} PSD(x, y, z, f)d(f). \quad (4)$$

The cross-plane contours of e_f for the frequency bands centered at $[f_{L,1}, f_{c,0}] = [30, 1000]$ Hz with a varying width of $\Delta f = [10, 100]$ Hz to minimize measurement noise, are shown in Fig. 16(a). For the low-frequency peaks at $f_{L,1} = 30$ Hz (see Fig. 16(a.1)), asymmetric distribution of disturbance energy with respect to the center-plane is found (referred to as '*asymmetric mode*'), with local maxima around the shear layers of the MLS close to the symmetry plane and in the wall-normal shear layer of the CLs on the negative spanwise sides. As found by the stability analysis [13,60], the asymmetric mode leads to a sinuous modulation of the low-speed regions. The high-frequency peak at $f_{c,0} = 1000$ Hz shows local maxima in e_f at the shear layer locations above all of the low-speed regions (Fig. 16(a.2)). The distribution at this higher frequency exhibits a greater spanwise symmetry with respect to the wake center (referred to as '*symmetric mode*'), indicating the growth of K-H instability [9]. Because of the considerably higher level of disturbance energy produced by the high-frequency peak, one can conclude that the K-H instability dominates the growth of disturbances at $\lambda_z/k = 8$.

For the case of reduced spanwise spacing of $\lambda_z/k = 6$ (Fig. 15(b)), a peak at $f_{c,0} = 190$ Hz along with its harmonics dominates the power spectrum at each low-speed region. The high-frequency peak corresponding to the vortex shedding around 1000 Hz reduces significantly. The increase in the broadband energy with respect to the undisturbed boundary layer is more uniform than that of the $\lambda_z/k = 8$ case for the MLS, in agreement with the faster disturbance growth and early onset of transition. The peak frequency of 190 Hz is close to that of the TS wave. Consequently, it is conjectured that the onset of transition is related to the amplification of TS wave by the presence of cylinder array. The disturbance energy (e_f) of the frequency band centered at $f_{c,0} = 190$ Hz and its third harmonics at $f_{c,3} = 760$ Hz is calculated with $\Delta f = [20, 20]$ Hz, as shown in Fig. 16(b). The disturbance energy distributions for both frequencies demonstrate nearly symmetric patterns with respect to the center plane, indicating the dominant role of the K-H instability during the transition process.

5.3. Single array with three cylinders

When three cylinders are placed in the array, two MLSs with high velocity deficit are produced (recall Fig. 9). The coexistence and interaction of the two MLSs may further facilitate the growth of asymmetric disturbances [46]. For the spanwise spacing of $\lambda_z/k = 8$ (Fig. 17(a)), the PSD exhibits two low frequency peaks of $f_{L,1} = 80$ Hz and $f_{L,2} = 130$ Hz and their harmonics, being amplified along the MLSs. The harmonics of the low frequency peaks show high amplitudes up to 10 kHz. A high frequency peak similar to the vortex shedding frequency of $f_{c,0} = 1000$ Hz for the isolated cylinder is also observed, being coupled with the harmonics of $f_{L,1}$ and $f_{L,2}$. These peaks reach comparable power levels.

To characterize the velocity fluctuation distribution for the low and high frequency peaks, the disturbance energy (e_f) in the frequency bands centered on $f = [80, 130, 1000]$ Hz is calculated with $\Delta f = [10, 20, 100]$ Hz, as shown in Fig. 18(a). The maxima of the disturbance energy corresponding to the low frequency peaks at $f_{L,1} = 80$ Hz and $f_{L,2} = 130$ Hz are located at the shear layer of the MLS and the CLs on the negative and positive spanwise side, respectively (see Fig. 18(a.1)(a.2)), yielding an asymmetric distribution along the span. The more pronounced asymmetric activity and higher PSD amplitude compared with the two cylinder cases indicate a stronger sinuous modulation of the low-speed regions. For the vortex shedding frequency of $f_{c,0} = 1000$ Hz, local maxima are present at the three-dimensional shear layer of all of the low-speed regions, as shown in Fig. 18(a.3). The pattern of disturbance energy demonstrates a fully symmetric distribution.

For the lower spanwise spacing of $\lambda_z/k = 6$ (Fig. 17(b)), a broadband amplitude increase is observed for the PSD for all low-speed regions compared with larger spanwise spacing, indicating a faster disturbance growth. The spectral peaks associated with the vortex shedding appear at a lower frequency of $f_{c,0} = 750$ Hz for both MLSs. This is due to the increased velocity deficit and vorticity thickness of the shear layer [61]. The disturbance energy distributions at $f = [750, 1500]$ Hz are calculated with $\Delta f = [100, 100]$ Hz, as shown in Fig. 18(b). The local peaks of the energy at 750 Hz are located along the wall-normal and spanwise shear layers of the MLSs, exhibiting good spanwise symmetry. The disturbance mode amplitude and pattern suggest the dominance of the symmetric instability mode for this condition.

5.4. Symmetry of disturbance energy

In order to quantitatively estimate the contribution of the symmetric and asymmetric modes to the growth of unsteady disturbances and the process of laminar to turbulent transition, the streamwise evolution of the disturbance energy within a narrow band surrounding the peak

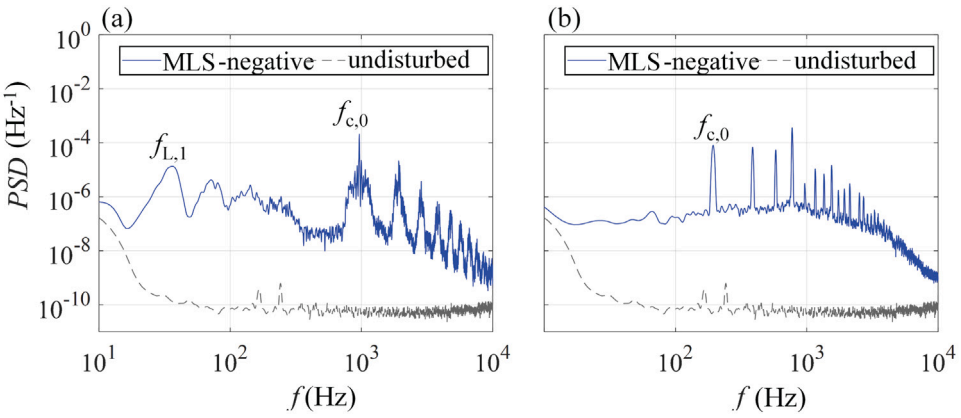

Fig. 15. Power spectra obtained at $x_s/k = 32$ for a single array with two cylinders, (a) $\lambda_z/k = 8$ and (b) $\lambda_z/k = 6$.

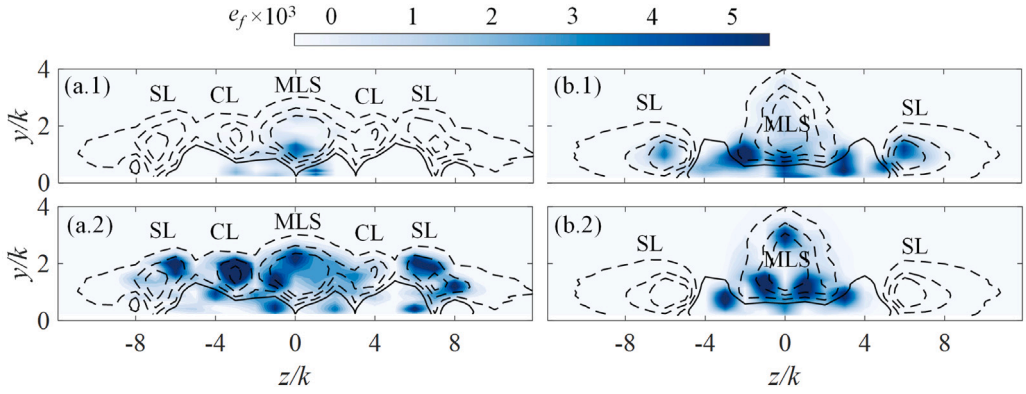

Fig. 16. Cross-plane contour of disturbance energy e_f at $x_s/k = 32$ of selected frequency bands for two cylinder configurations with (a) $\lambda_z/k = 8$ and (b) $\lambda_z/k = 6$; (a.1) f = 30 Hz, (a.2) f = 1000 Hz, (b.1) f = 190 Hz, (b.2) f = 760 Hz.

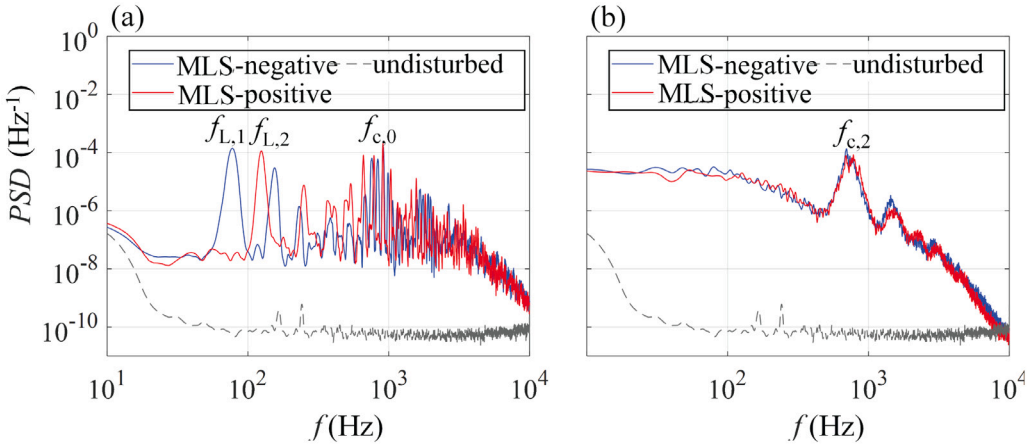

Fig. 17. Power spectra obtain at $x_s/k = 32$ for a single array with three cylinders, (a) $\lambda_z/k = 8$ and (b) $\lambda_z/k = 6$.

frequency and integrated over the entire wake span (e_{rms}) is computed at all measurement stations. Here, e_{rms} is defined as [9] :

$$e_{rms}(f) = \iiint_{f-\Delta f}^{f+\Delta f} PSD(x, y, z, f)d(f)d(\frac{y}{k})d(\frac{z}{k}). \quad (5)$$

The peak frequencies for each roughness distribution and the corresponding mode type are summarized in Table 3. For the smaller spanwise interval of $\lambda_z/k = 6$, only the symmetric type of disturbance modes appears in the wake, indicating its exclusive role in the disturbance growth that leads to transition. For $\lambda_z/k = 8$, both symmetric and asymmetric modes are amplified. The streamwise evolution of the e_{rms} for different peak frequencies is plotted in Fig. 19 for the larger spanwise interval ($\lambda_z/k = 8$).

Table 3
Category of the frequency peaks for all the configurations.

Roughness distribution	$N_{symmetry}$	$N_{asymmetry}$
Single array-N2-8k	$f_{c,0}$ = 1000 Hz	$f_{L,1}$ = 30 Hz; $f_{L,1}$ = 50 Hz
Single array-N2-6k	$f_{c,0}$ = 190 Hz	–
Single array-N3-8k	$f_{c,0}$ = 1000 Hz	$f_{L,1}$ = 80 Hz; $f_{L,1}$ = 130 Hz
Single array-N3-6k	$f_{c,2}$ = 750 Hz	–

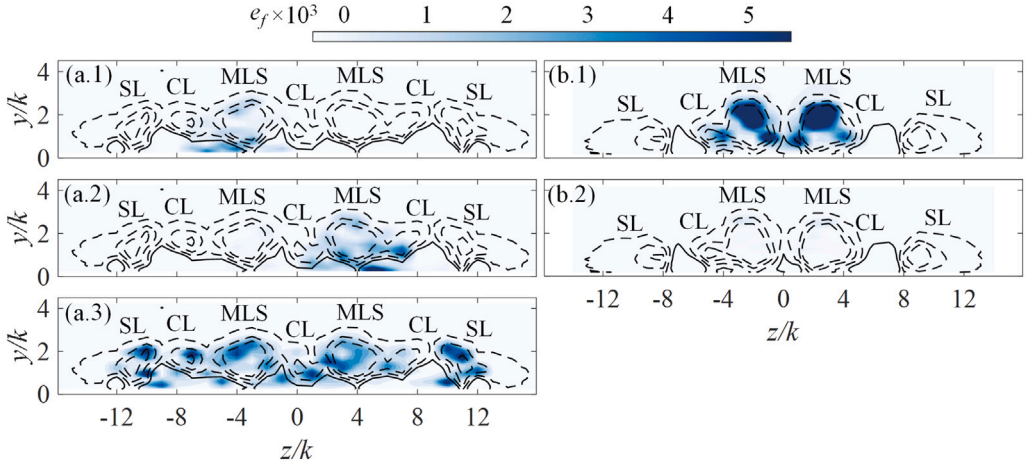

Fig. 18. Cross-plane contour of disturbance energy e_f at $x_s/k = 32$ of selected frequency bands for three cylinder configurations with (a) $\lambda_z/k = 8$ and (b) $\lambda_z/k = 6$; (a.1) $f = 80$ Hz, (a.2) $f = 130$ Hz, (a.3) $f = 1000$ Hz, (b.1) $f = 750$ Hz, (b.2) $f = 1500$ Hz.

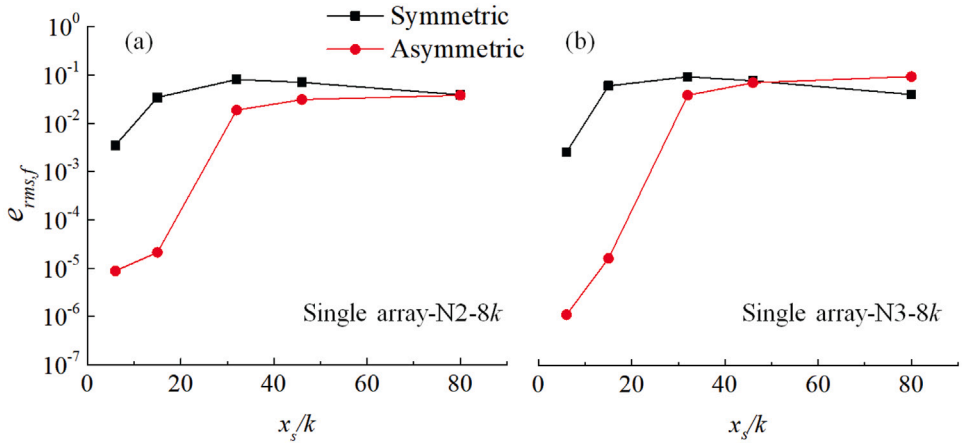

Fig. 19. Streamwise evolution of integrated disturbance energy e_{rms} at selected frequency bands for a single array with (a) two and (b) three cylinders for $\lambda_z/k = 8$.

For the array of two cylinders (Fig. 19(a)), the symmetric disturbances exhibit significantly higher disturbance energy than the asymmetric mode at the upstream measurement locations of $x_s/k = 6$ and $x_s/k = 15$. For $x_s/k > 32$, the disturbance energy in the symmetric mode decreases with downstream distance, albeit rather slowly. On the other hand, the energy of the asymmetric mode continues to increase throughout the range of measurement and eventually becomes equal in energy to the symmetric mode at the most downstream station.

When three cylinders are arranged in the array (Fig. 19(b)), the symmetric mode continues to dominate the disturbance energy during the upstream stage, but the $e_{rms}(f)$ for the asymmetric disturbances continues its exponential growth even after the saturation of the symmetric mode and eventually reaches an even higher level of disturbance energy. Consequently, the dominant instability mode switches over from the higher frequency K-H mode to an asymmetric mode with low peak frequency. The latter is expected to play an important role in the onset of transition.

6. Conclusion

In the present research, we investigated the effect of distributed roughness elements on laminar to turbulent transition over a NACA 0012 airfoil at a chord Reynolds number of 1.44×10^5. The effects of spanwise and streamwise interaction between the various elements for a given roughness distribution are investigated in a systematic manner experimentally. The transitional flow features behind spanwise arrays of equally spaced cylindrical roughness elements are addressed. The velocity and temperature fields within the wake region behind the roughness distribution have been measured with hotwire anemometry and infrared thermography, respectively. Both streamwise and spanwise interactions between the roughness elements have been studied by placing the elements in three different configurations: an isolated roughness element, a single array of roughness elements, and a pair of arrays in stagger.

The spanwise interaction between the roughness elements leads to connections and an eventual merging between the neighboring low-speed regions within the wake of the array, resulting in a modification of the velocity streak pattern as well as the streak amplitude evolution. The maximum spanwise interval that causes an effective spanwise interaction across the array is equal to twice the roughness diameter (i.e., $\lambda_z/k = 8$). The addition of a second array of roughness elements leads to a significant increase in the amplitude of the merged low-speed regions. However, transition onset is promoted and delayed $\lambda_z/k = 8$ and 6, respectively, indicating the strong dependence on the spanwise wavelength. The underlying instability mechanisms remain the same as those for a single array.

A critical streak amplitude of 0.42 is identified, above which transition can be promoted. The maximum effect on transition onset is observed when two neighboring low-speed regions overlap close to the roughness, which occurs for $\lambda_z/k = 6$ in the current experiment. The merged low-speed regions lead to the amplification of unsteady disturbances along the surrounding three-dimensional shear layer and promote an earlier laminar-turbulent transition.

Spectral analysis of the velocity fluctuations identifies the frequency associated with the peak growth of unsteady disturbances. The measurements reveal two main types of disturbance modes corresponding to symmetric and asymmetric distributions, respectively, of the streamwise velocity fluctuations. The dominant disturbance mode leading to transition is determined by the number and the spanwise spacing of the roughness elements. When an odd number of merged low-speed regions are produced in the wake, the symmetric mode related to the Kelvin–Helmholtz instability dominates the growth of disturbances near the surrounding shear layer. Differently, for an even number of merged low-speed regions, the asymmetric mode undergoes a faster growth, playing the dominant role on disturbance growth at the larger spanwise spacing of $\lambda_z/k = 8$. For smaller spanwise spacing of $\lambda_z/k = 6$, although the asymmetric disturbances appear in the near wake, their intensity decays substantially before the inception of the turbulent wedge, resulting in an insignificant role of the asymmetric disturbances during the transition process.

CRediT authorship contribution statement

Qingqing Ye: Writing – review & editing, Writing – original draft, Visualization, Validation, Methodology, Investigation. **Francesco Avallone:** Writing – review & editing, Writing – original draft, Validation, Methodology, Investigation. **Daniele Ragni:** Writing – review & editing, Validation, Methodology, Investigation. **Damiano Casalino:** Writing – review & editing, Validation, Investigation.

Declaration of competing interest

The authors declare that they have no known competing financial interests or personal relationships that could have appeared to influence the work reported in this paper.

Acknowledgments

This research has been supported by the National Natural Science Foundation of China (No. 12372280), National Key R&D Program of China (No. 2020YFA0405700).

Data availability

Data will be made available on request.

References

[1] S.P. Schneider, Developing mechanism-based methods for estimating hypersonic boundary-layer transition in flight: The role of quiet tunnels, Prog. Aerosp. Sci. 72 (2015) 17–29.
[2] M. Choudhari, F. Li, C.-L. Chang, J. Edwards, M. Kegerise, R. King, Laminar-turbulent transition behind discrete roughness elements in a high-speed boundary layer, AIAA Paper 2010- 1575, 2010.
[3] D.K. Puckert, U. Rist, Experiments on critical reynolds number and global instability in roughness-induced laminar–turbulent transition, J. Fluid Mech. 844 (2018) 878–904.
[4] S.P. Schneider, Effects of roughness on hypersonic boundary-layer transition, J. Spacecr. Rocket. 45 (2) (2008) 193–209.
[5] S. Min, K. Yee, New roughness-induced transition model for simulating ice accretion on airfoils, AIAA J. 51 (1) (2021) 250–262.
[6] J.P. Bons, A Review of Surface Roughness Effects in Gas Turbines, J. Turbomach. 132 (2) (2010) 021004.
[7] B. Bornhoft, S.S. Jain, K. Goc, S.T. Bose, P. Moin, Large-eddy simulations of the NACA23012 airfoil with laser-scanned ice shapes, Aerosp. Sci. Technol. 146 (2024) 108957.
[8] J.H.M. Fransson, L. Brandt, A. Talamelli, C. Cossu, Experimental and theoretical investigation of the nonmodal growth of steady streaks in a flat plate boundary layer, Phys. Fluids 16 (10) (2004) 3627–3638.
[9] F.G. Ergin, E.B. White, Unsteady and transitional flows behind roughness elements, AIAA J. 44 (11) (2006) 2504–2514.
[10] P. Andersson, M. Berggren, D.S. Henningson, Optimal disturbances and bypass transition in boundary layers, Phys. Fluids 11 (1) (1999) 134–150.
[11] E. Reshotko, Transient growth: A factor in bypass transition, Phys. Fluids 13 (5) (2001) 1067–1075.
[12] M.T. Landahl, On sublayer streaks, J. Fluid Mech. 212 (1990) 593–614.
[13] J.-C. Loiseau, J.-C. Robinet, S. Cherubini, E. Leriche, Investigation of the roughness-induced transition: Global stability analyses and direct numerical simulations, J. Fluid Mech. 760 (2014) 175–211.
[14] M. Choudhari, P. Fischer, Roughness-induced transient growth, AIAA Paper 2005-4765, 2005.
[15] C.-L. Chang, M.M. Choudhari, F. Li, Numerical computations of hypersonic boundary-layer over surface irregularities, AIAA Paper 2010- 1572, 2010.
[16] Q. Ye, F.F.J. Schrijer, F. Scarano, Boundary layer transition mechanisms behind a micro-ramp, J. Fluid Mech. 793 (2016) 132–161.
[17] Q. Ye, F.F.J. Schrijer, F. Scarano, Geometry effect of isolated roughness on boundary layer transition investigated by tomographic piv, Int. J. Heat Fluid Fl. 61 (Part A) (2016) 31–44.
[18] Q. Ye, F.F.J. Schrijer, F. Scarano, On reynolds number dependence of micro-ramp-induced transition, J. Fluid Mech. 837 (2018) 597–626.
[19] L.H. von Deyn, P. Forooghi, B. Frohnapfel, P. Schlatter, A. Hanifi, D.S. Henningson, Direct numerical simulations of bypass transition over distributed roughness, AIAA J. 58 (2) (2020) 702–711.
[20] S. Drews, R. Downs, C. Doolittle, D. Goldstein, E. White, Direct numerical simulations of flow past random distributed roughness, AIAA Paper 2011- 564, 2011.
[21] S. Muppidi, K. Mahesh, Direct numerical simulations of roughness-induced transition in supersonic boundary layers, J. Fluid Mech. 693 (2012) 28–56.
[22] M.M. Choudhari, F. Li, P. Paredes, L. Duan, Effect of 3D Roughness Patch on Instability Amplification in a Supersonic Boundary Layer, AIAA Paper 2019-0877, 2019.
[23] B.H. Carmichael, Critical Reynolds numbers for multiple three dimensional roughness elements, Report NAI-58-589 (BLC-112), Northrop Aircraft, Inc.,, Hawthorne, CA, 1958.
[24] A. Chou, M.A. Kegerise, R.A. King, Transition induced by streamwise arrays of roughness elements on a flat plate in mach 3.5 flow, J. Fluid Mech. 888 (2020) 1–34.
[25] R. Ma, K. Mahesh, Boundary layer transition due to distributed roughness: Effect of roughness spacing, J. Fluid Mech. 977 (2023) A27.
[26] J.H.M. Fransson, A. Talamelli, On the generation of steady streamwise streaks in flat-plate boundary layers, J. Fluid Mech. 698 (2012) 211–234.
[27] J.R. Brinkerhoff, M.I. Yaras, Numerical investigation of transition in a boundary layer subjected to favourable and adverse streamwise pressure gradients and elevated free stream turbulence, J. Fluid Mech. 781 (2015) 52–86.
[28] M.J.P. Hack, T.A. Zaki, Streak instabilities in boundary layers beneath free-stream turbulence, J. Fluid Mech. 741 (2014) 280–315.
[29] M.F. Kerho, M.B. Bragg, Airfoil boundary-layer development and transition with large leading-edge roughness, AIAA J. 35 (1) (1997) 75–84, http://dx.doi.org/10.2514/2.65.
[30] C.M. Langel, R. Chow, C.P. Van Dam, M.A. Rumsey, D.C. Maniaci, R.S. Ehrmann, E.B. White, A Computational Approach to Simulating the Effects of Realistic Surface Roughness on Boundary Layer Transition, AIAA Paper 2014- 0234, 2014, http://dx.doi.org/10.2514/6.2014-0234.
[31] E. Justiniano, L.M. Brown, E.B. White, S. Suryanarayanan, D.B. Goldstein, Mitigation of roughness-induced boundary-layer transition on airfoils using shielding strips, AIAA J. 62 (7) (2024) 2476–2488, http://dx.doi.org/10.2514/1.J063590.
[32] R. Merino-Martinez, A.R. Carpio, L.T.L. Pereira, S. van Herk, F. Avallone, D. Ragni, M. Kotsonis, Aeroacoustic design and characterization of the 3D-printed, open-jet, anechoic wind tunnel of delft university of technology, Appl. Acoust. 170 (2020) 107504.
[33] A.E. Von Doenhoff, A.L. Braslow, The effect of distributed surface roughness on laminar flow, in: G.V. Lachmann (Ed.), In Boundary Layer and Flow Control, Pergamon, 1961, pp. 657–681.
[34] G.M. Carlomagno, G. Cardone, Infrared thermography for convective heat transfer measurements, Exp. Fluids 49 (6) (2010) 1187–1218.
[35] F. Avallone, F.F.J. Schrijer, G. Cardone, Infrared thermography of transition due to isolated roughness elements in hypersonic flows, Phys. Fluids 28 (2) (2016) 024106.
[36] T.P. Chong, P. Joseph, "Ladder" structure in tonal noise generated by laminar flow around an airfoil, J. Acoust. Soc. Am. 131 (6) (2012) 461–467.
[37] P.S. Iyer, K. Mahesh, High-speed boundary-layer transition induced by a discrete roughness element, J. Fluid Mech. 729 (2013) 524–562.
[38] F. Avallone, Q. Ye, F.F.J. Schrijer, F. Scarano, G. Cardone, Tomographic piv investigation of roughness-induced transition in a hypersonic boundary layer, Exp. Fluids 55 (11) (2014) 1852.
[39] A. Chou, R.A. King, M.A. Kegerise, Transition induced by an egg-crate roughness on a flat plate in supersonic flow, AIAA Paper 2020- 3045, 2020.
[40] J.A. Redford, N.D. Sandham, G.T. Roberts, Numerical simulations of turbulent spots in supersonic boundary layers: Effects of mach number and wall temperature, Prog. Aerosp. Sci. 52 (2012) 67–79.
[41] M.S. Kuester, E.B. White, Structure of turbulent wedges created by isolated surface roughness, Exp. Fluids 57 (4) (2016) 47.

[42] C. Nicolai, S. Tadde, C. Manes, B. Ganapathisubramani, Wakes of wall-bounded turbulent flows past patches of circular cylinders, J. Fluid Mech. 892 (2020) A37.
[43] J. Zhou, S.K. Venayagamoorthy, Near-field mean flow dynamics of a cylindrical canopy patch suspended in deep water, J. Fluid Mech. 858 (2019) 634–655.
[44] A. Nasr, J.C.S. Lai, Two parallel plane jets: mean flow and effects of acoustic excitation, Exp. Fluids 22 (3) (1997) 251–260.
[45] S. Zhong, T.P. Chong, H.P. Hodson, A comparison of spreading angles of turbulent wedges in velocity and thermal boundary layers, J. Fluids Eng. 125 (2003) 8.
[46] M.M. Choudhari, F. Li, P. Paredes, Effect of distributed patch of smooth roughness elements on transition in a high-speed boundary layer, AIAA Paper 2018- 3532, 2018.
[47] N.R. Vadlamani, P.G. Tucker, P. Durbin, Distributed roughness effects on transitional and turbulent boundary layers, Flow Turbul. Combust. 100 (2018) 627–649.
[48] A.M. Hamed, M. Sadowski, Z. Zhang, L.P. Chamorro, Transition to turbulence over 2d and 3d periodic large-scale roughnesses, J. Fluid Mech. 804 (2016) R6.
[49] P. Andersson, L. Brandt, A. Bottaro, D.S. Henningson, On the breakdown of boundary layer streaks, J. Fluid Mech. 428 (2001) 29–60.
[50] P. Paredes, M.M. Choudhari, F. Li, Instability wave–streak interactions in a supersonic boundary layer, J. Fluid Mech. 831 (2017) 524–553.
[51] A. Chou, R.A. King, M.A. Kegerise, Transition induced by tandem rectangular roughness elements on a supersonic flat plate, AIAA Paper 2018- 3531, 2018.
[52] J.A. Redford, N.D. Sandham, G.T. Roberts, Compressibility effects on boundary-layer transition induced by an isolated roughness element, AIAA J. 48 (12) (2010) 2818–2830.
[53] M. Bernardini, S. Pirozzoli, P. Orlandi, S.K. Lele, Parameterization of boundary-layer transition induced by isolated roughness elements, AIAA J. 52 (10) (2014) 2261–2269.
[54] J.P. Van den Eynde, N.D. Sandham, Numerical simulations of transition due to isolated roughness elements at mach 6, AIAA J. 54 (1) (2015) 53–65.
[55] S. Shahinfar, J. Fransson, S. Sattarzadeh, A. Talamelli, Scaling of streamwise boundary layer streaks and their ability to reduce skin-friction drag, J. Fluid Mech. 733 (2013) 1–32.
[56] M.S. Acarlar, C.R. Smith, A study of hairpin vortices in a laminar boundary layer. Part 1. hairpin vortices generated by a hemisphere protuberance, J. Fluid Mech. 175 (1987) 1–41.
[57] E.B. White, F.G. Ergin, Receptivity and transient growth of roughness-induced disturbances, AIAA Paper 2003- 4243, 2003.
[58] N. De Tullio, P. Paredes, N.D. Sandham, V. Theofilis, Laminar–turbulent transition induced by a discrete roughness element in a supersonic boundary layer, J. Fluid Mech. 735 (2013) 613–646.
[59] X. Wang, X. Zhong, Receptivity of a hypersonic flat-plate boundary layer to three-dimensional surface roughness, J. Spacecr. Rockets 45 (6) (2008) 1165–1175.
[60] M. Asai, M. Minagawa, M. Nishioka, The instability and breakdown of a near-wall low-speed streak, J. Fluid Mech. 455 (2002) 289–314.
[61] M. Lesieur, Turbulence in Fluids: 4th Edition, Springer, Dordrecht, 2008, pp. 91–104.